



Cite this: DOI: 10.1039/d3cp05298b

# Enhancement and modulation of valley polarization in Janus CrSSe with internal and external electric fields†

Runxian Jiao,<sup>a</sup> Qingyuan Wei,<sup>a</sup> Lichuan Zhang,<sup>a</sup> Yuee Xie,<sup>a</sup> Jingjing He,<sup>\*b</sup> Yangbo Zhou,<sup>\*c</sup> Lei Shen<sup>d</sup> and Jiaren Yuan<sup>\*c</sup>

The valley polarization, induced by the magnetic proximity effect, in monolayer transition metal dichalcogenides (TMDCs), has attracted significant attention due to the intriguing fundamental physics. However, the enhancement and modulation of valley polarization for real device applications is still a challenge. Here, using first-principles calculations we investigate the valley polarization properties of monolayer TMDCs CrS<sub>2</sub> and CrSe<sub>2</sub> and how to enhance the valley polarization by constructing Janus CrSSe (with an internal electric field) and modulate the polarization in CrSSe by applying external electric fields. Janus CrSSe exhibits inversion symmetry breaking, internal electric field, spin–orbit coupling, and compelling spin–valley coupling. A magnetic substrate of the MnO<sub>2</sub> monolayer can induce a modest magnetic moment in CrSe<sub>2</sub>, CrS<sub>2</sub>, and CrSSe. Notably, the Janus structure with an internal electric field has a much larger valley  $\rho$  compared with its non-Janus counterparts. Moreover, the strength of valley polarization can be further modulated by applying external electric fields. These findings suggest that Janus materials hold promise for designing and developing advanced valleytronic devices.

Received 31st October 2023,  
Accepted 3rd April 2024

DOI: 10.1039/d3cp05298b

rsc.li/pccp

## 1 Introduction

Valley, a new degree of freedom, has emerged as a promising avenue with significant potential for information storage, processing, and transmission, offering faster processing speeds and lower energy consumption than conventional electronics.<sup>1</sup> The inherent breaking of spatial inversion symmetry and the strong spin–orbit coupling effect (SOC) in valley materials lead to the disruption of spin degeneracy in the non-equivalent  $K$  and  $K'$  valleys,<sup>2,3</sup> establishing a unique coupling between spin and valley. Furthermore, breaking the time inversion symmetry allows for the perturbation of carrier transport equilibrium within the non-equivalent  $K$  valley, resulting in valley polarization.<sup>4,5</sup> Given this unique physical property, numerous novel phenomena have been observed experimentally, including the valley Hall effect and valley-dependent optical selection rules,<sup>6,7</sup>

leading to the exploration of various device applications, such as valley spin valves and valley filters.<sup>3,8</sup>

Graphene is the first promising 2D material for valley polarization.<sup>9,10</sup> However, its semi-metallic nature hinders its integration into valleytronic devices. Unlike graphene, some new valley materials with band gaps have been proposed, such as MoS<sub>2</sub>,<sup>11–13</sup> SnS,<sup>9,14</sup> MoSi<sub>2</sub>N<sub>4</sub>, and TcIrGe<sub>2</sub>S<sub>6</sub>.<sup>15</sup> The transition metal dichalcogenides (TMDCs) with appropriate band gaps and Dirac-type valleys are suitable for valleytronic devices, which attracted widespread attention.<sup>12,16</sup> Recently, a new member of 2D TMDCs, Janus MoSSe, has been successfully synthesized and has attracted great attention.<sup>17</sup> Janus MoSSe is prepared from MoS<sub>2</sub>, on which an S-layer is replaced by Se atoms, breaking the out-of-plane structural symmetry. Such an asymmetric configuration provides additional freedom that plays a crucial role in introducing novel physical properties.<sup>17–23</sup> For instance, ZrSSe exhibits excellent optical properties,<sup>24</sup> and MoSSe displays a strong Rashba effect.<sup>25,26</sup> Additionally, the Janus structures show a strong valley polarization effect and a large valley polarization compared to the common TMDCs.<sup>27,28</sup>

The essence of utilizing the valley as an information carrier is to eliminate valley degeneracy, thereby inducing valley polarization. In recent years, several methods for generating valley polarization have been proposed, including optical pumping,<sup>29–31</sup> breaking the crystal symmetry,<sup>32</sup> applied magnetic fields,<sup>33,34</sup> magnetic atom doping,<sup>35,36</sup> and the magnetic proximity effect.<sup>10,11,13,37–43</sup> Among them, the magnetic proximity effect is a particularly effective and

<sup>a</sup> School of Physics and Electronic Engineering, Jiangsu University, Zhenjiang 212013, China

<sup>b</sup> College of Information Science and Technology, Nanjing Forestry University, Nanjing 210037, China. E-mail: hejj@njfu.edu.cn

<sup>c</sup> School of Physics and Materials Science, Nanchang University, Nanchang 330031, China. E-mail: yangbozhou@ncu.edu.cn, jryuan@ncu.edu.cn

<sup>d</sup> Department of Mechanical Engineering, National University of Singapore, 9 Engineering Drive 1, Singapore 117542, Singapore

† Electronic supplementary information (ESI) available. See DOI: <https://doi.org/10.1039/d3cp05298b>

accessible method for introducing large valley polarization in valley-polarized materials. For instance, the magnetic proximity effect of ferromagnetic substrates, such as  $\text{Fe}_3\text{GeTe}_2$ ,<sup>11</sup>  $\text{MnPS}_3$ ,<sup>10</sup> yttrium iron garnet,<sup>43</sup>  $\text{ScI}_2$ ,<sup>42</sup>  $\text{CoO}$ , and  $\text{MnO}$ ,<sup>44,45</sup> induces large valley polarization.

In the present work, we employ first-principles calculations to explore the electronic structure and valley polarization properties of transition metal dichalcogenides  $\text{CrX}_2$  ( $\text{X} = \text{S}, \text{Se}$ ) and the Janus structure  $\text{CrSSe}$ . The results demonstrate that the monolayer Janus structure  $\text{CrSSe}$  is an exceptional candidate with inherent spin-valley coupling. Moreover, a more significant valley polarization of Janus  $\text{CrSSe}$  is obtained with an  $\text{MnO}_2$  magnetic substrate than that of  $\text{CrS}_2$  and  $\text{CrSe}_2$  under identical conditions. The monolayer Janus structure  $\text{CrSSe}$  undergoes evident polarization upon incorporating a magnetic substrate, thus paving the way for a new platform in the advancement of valleytronics.

## 2 Computational methods

We performed first-principles calculations using the software package Vienna *Ab initio* Simulation Package (VASP)<sup>46</sup> based on density functional theory. The Perdew–Burke–Ernzerhof (PBE) function was selected as the exchange–correlation function.<sup>47,48</sup> To avoid artificial periodic interactions, a vacuum space larger than 25 Å was adopted. The cutoff energy of the plane wave was set to 500 eV. In structural optimization and electronic structure calculations,  $15 \times 15 \times 1$  and  $18 \times 18 \times 1$  K-grid densities were used in the first Brillouin zone, respectively. The convergence thresholds for energy and force were set at less than  $10^{-5}$  eV and  $0.01 \text{ eV Å}^{-1}$ , respectively. The DFT-D3 van der Waals correction and Coulomb interaction<sup>49</sup> of  $U_{\text{eff}} = 3.9 \text{ eV}$  for Mn 3d orbitals were applied in the  $\text{CrX}_2/\text{MnO}_2$  heterostructure calculations.<sup>50</sup> The Berry curvature of monolayer  $\text{CrSSe}$  was performed by the maximally localized Wannier function method, implemented in the WANNIER90 package.<sup>51</sup> The phonon dispersion spectrum was calculated using PHONOPY software based on density functional perturbation theory with a  $3 \times 3 \times 1$  supercell.<sup>52</sup>

## 3 Results and discussion

The optimized atomic structure of Janus  $\text{CrSSe}$  is shown in Fig. 1(a). Through the calculation, it can be found that  $\text{CrSSe}$  is a non-magnetic semiconductor like  $\text{CrS}_2$  and  $\text{CrSe}_2$ .<sup>53</sup> The Janus structure is derived from the monolayer  $\text{CrS}_2$  by replacing the bottom S atoms with Se. The bond length of Cr–Se (2.421 Å) is slightly longer than that of Cr–S (2.300 Å) in Janus  $\text{CrSSe}$ . The point group of hexagonal  $\text{CrS}_2$ , denoted as  $D_{3h}$  transforms the triangular  $C_{3v}$  symmetry for Janus  $\text{CrSSe}$  due to the breaking of mirror symmetry upon Se substitution. The relaxed lattice constants of  $\text{CrS}_2$ ,  $\text{CrSe}_2$ , and  $\text{CrSSe}$  are 3.04 Å, 3.21 Å, and 3.12 Å, respectively. As can be seen, the lattice constant of Janus  $\text{CrSSe}$  is in between  $\text{CrS}_2$  and  $\text{CrSe}_2$ .

Fig. 1b shows the phonon band structure, which has no apparent imaginary frequency in the entire Brillouin zone (BZ),

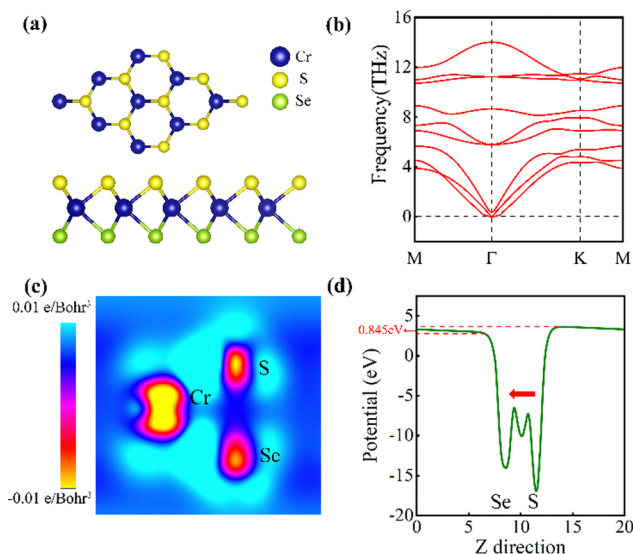


Fig. 1 (a) Schematic crystal structure of the optimized  $\text{CrSSe}$ , with yellow, green, and blue spheres representing S, Se, and Cr atoms, respectively. (b) Phonon spectrum of monolayer  $\text{CrSSe}$ . (c) Charge difference density. (d) Electrostatic potential distribution along the Z-direction.

verifying the dynamic stability of Janus  $\text{CrSSe}$ . Additionally, we calculate the formation energy to evaluate its energetic stability, employing the following formula:<sup>54</sup>

$$E_f = E_{\text{total}} - E_{\text{Cr}} - E_{\text{S}} - E_{\text{Se}} \quad (1)$$

where  $E_{\text{total}}$  is the energy of monolayer  $\text{CrSSe}$ , and  $E_{\text{Cr}}$ ,  $E_{\text{Se}}$ , and  $E_{\text{S}}$  are the energy of single atom Cr, Se, and S, respectively. The calculated formation energies of  $\text{CrS}_2$ ,  $\text{CrSe}_2$ , and  $\text{CrSSe}$  are  $-7.66$ ,  $-8.05$  and  $-7.43 \text{ eV}$  per unit cell, respectively. These results indicate that Janus  $\text{CrSSe}$  has excellent energy stability as its parents.

Fig. 1c shows the charge density difference of  $\text{CrSSe}$  on the  $[110]$  crystal face. The charge density distributions are noticeably different between the Se and S atomic layers. Specifically, the charge is more concentrated around the S atom than around the Se atom. Furthermore, a Bader charge analysis is performed to provide further insights into the charge transfer process of the Janus  $\text{CrSSe}$  system. The S atom obtains  $0.53 e$  from the Cr atom, and the Se atom gains  $0.39 e$  from the Cr atom. The trend aligns with the electronegativity sequence of  $\text{S} > \text{Se} > \text{Cr}$ . This indicates the occurrence of charge rearrangement in the  $\text{CrSSe}$  system.

Fig. 1d presents the average electrostatic potential along the Z direction in Janus  $\text{CrSSe}$ . The red arrow's direction indicates the local electrostatic potential between Cr and Se (S) atoms. The vacuum energy level distributions between the upper and lower surfaces are different, which signifies the work function distribution is different. The lower potential distribution and higher work function on the S atom side reflect the greater electronegativity compared with Se. These results indicate that a built-in electric field from Se to S is established in Janus  $\text{CrSSe}$ .

Fig. 2 shows the band structures of  $\text{CrS}_2$ ,  $\text{CrSe}_2$ , and  $\text{CrSSe}$  with spin-orbit coupling (SOC).  $\text{CrS}_2$ ,  $\text{CrSe}_2$ , and  $\text{CrSSe}$  are non-magnetic

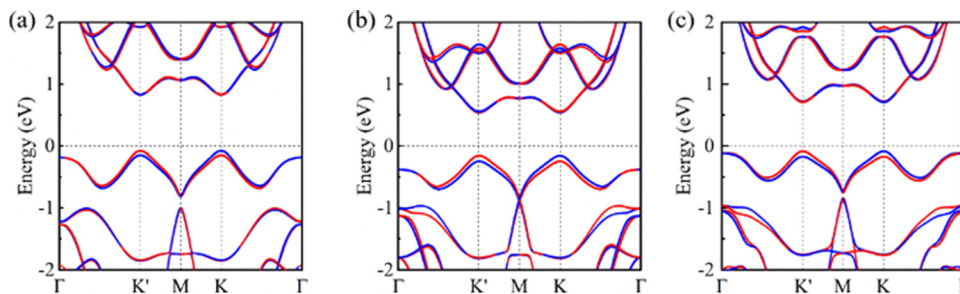


Fig. 2 (a) Energy band diagrams of  $\text{CrS}_2$ , (b)  $\text{CrSe}_2$ , and (c)  $\text{CrSSe}$  considering spin–orbit coupling (SOC), the red and blue lines correspond to spin-up and spin-down.

semiconductors that are consistent with previous research results.<sup>53</sup> The valence band maximum (VBM) and conduction band minimum (CBM) are located at the  $K/K'$  valley, highlighting their direct bandgap semiconducting nature. The band gaps of  $\text{CrS}_2$ ,  $\text{CrSe}_2$ , and  $\text{CrSSe}$  are 0.91 eV, 0.70 eV, and 0.79 eV, respectively. Due to the strong spin–orbit coupling, notable spin splitting (69 meV, 90 meV, and 81 meV) appears at the  $K$  and  $K'$  valleys near the VBM for  $\text{CrS}_2$ ,  $\text{CrSe}_2$ , and the Janus  $\text{CrSSe}$  monolayer, respectively. The upper (lower) band is dominated by the spin-down (spin-up) component at the  $K$  point and the spin-up (spin-down) component at the  $K'$  point, indicating spin-valley coupling. However, the presence of time-reversal symmetry ensures that the energy of the  $K$  and  $K'$  valleys remains energetically degenerate.

To induce the valley polarization, a magnetic substrate is introduced to provide a magnetic proximity effect. Here, we choose semiconducting  $\text{MnO}_2$  as the magnetic substrate, which has been reported as a two-dimensional magnetic semiconductor with intrinsic ferromagnetism.<sup>55</sup> We constructed a  $\text{CrSSe}/\text{MnO}_2$  heterojunction, which breaks the time-reversal symmetry

and allows the manipulation of valley polarization in the  $\text{CrSSe}$  monolayer. The introduced magnetic substrate produces a distinct energy difference between the  $K$  and  $K'$  valleys, leading to valley polarization at  $K$  and  $K'$ . The magnitude of the valley polarization is defined as the energy difference between the extreme of the valence band between  $K$  and  $K'$  valleys, denoted as  $\Delta_{KK'} = E_K - E_{K'}$ . Fig. 3 shows the six heterojunction models with different stacking orders when Se atoms are located at the contact interface. Diverse stacking arrangements produced a wide range of valley polarization, ranging from 2 to 80 meV, as listed in the ESI,<sup>†</sup> Table S1. It is indicated that the stacking configuration directly affects the coupling between magnetic atoms and transition metal ions, significantly influencing valley polarization. When S atoms are located at the contact interface as shown in the ESI,<sup>†</sup> Fig. S1, the valley polarization ranges from 8 to 23 meV (Fig. S2, ESI<sup>†</sup>), which is smaller than that for Se at the interface. Hence, we chose the II stacking configuration when Se is close to the interface with the most stable structure. Fig. 4 illustrates the spin projection bands with SOC for the  $\text{CrS}_2/\text{MnO}_2$ ,  $\text{CrSe}_2/\text{MnO}_2$ , and  $\text{CrSSe}/\text{MnO}_2$

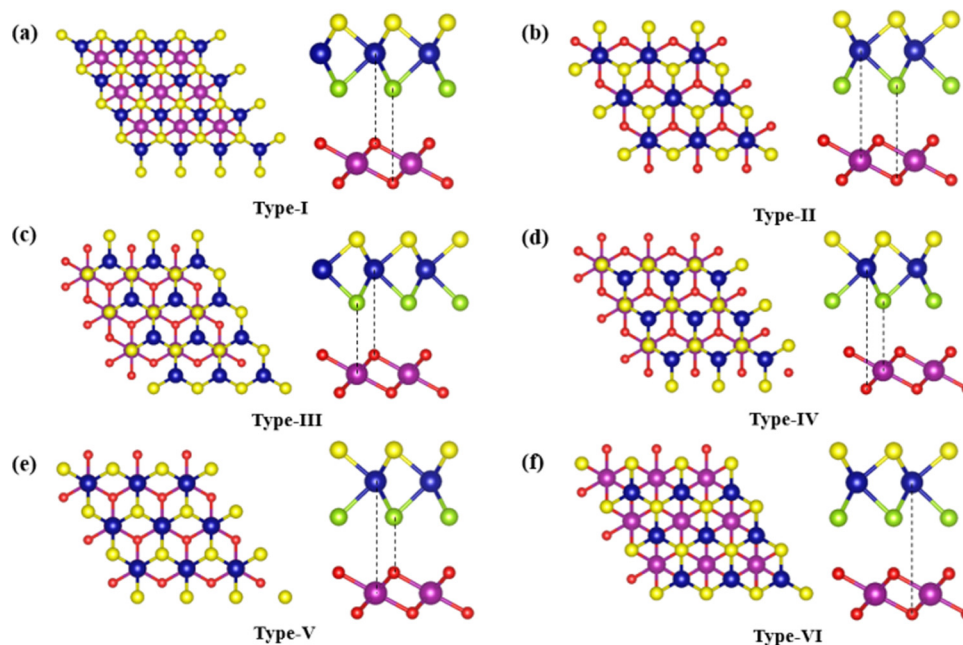


Fig. 3  $\text{CrSSe}/\text{MnO}_2$  heterojunction with different stacking orders.

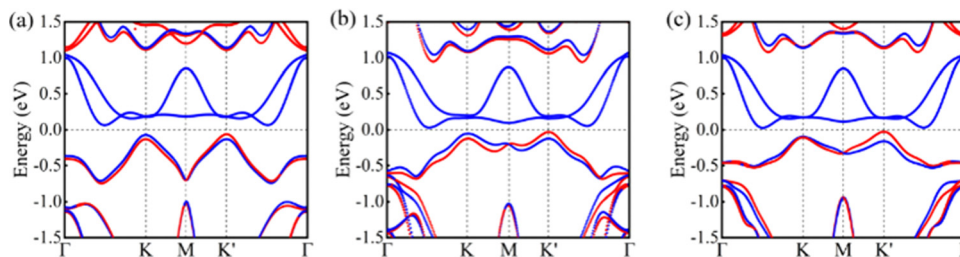


Fig. 4 The spin projected band structure of (a)  $\text{CrS}_2/\text{MnO}_2$ , (b)  $\text{CrSe}_2/\text{MnO}_2$ , (c)  $\text{CrSSe}/\text{MnO}_2$ .

heterojunctions. The valley polarization of the initial valence band is 8, 20, and 71 meV, respectively. Hence, valley polarization is significantly amplified in the Janus monolayer.

To unravel the intrinsic mechanism of the enhanced valley polarization in the Janus system, we calculate the charge density difference of  $\text{CrS}_2/\text{MnO}_2$ ,  $\text{CrSe}_2/\text{MnO}_2$ , and  $\text{CrSSe}/\text{MnO}_2$  heterojunctions to analyse the coupling effect between chromium dichalcogenides and the magnetic substrate.<sup>56,57</sup> As shown in Fig. 5a–c, one can notice that the charges are accumulated on the  $\text{MnO}_2$  and the TMDC sides, suggesting substantial charge transfer from the TMDCs to the  $\text{MnO}_2$  substrate. The planar average charge density difference  $\rho(z)$  in the vertical direction reveals a significant disparity in charge distribution, as shown in Fig. 5d–f. Notably,  $\text{MnO}_2$  exhibits a positive charge density, while the TMDCs display a negative charge density, confirming the occurrence of charge transfer between the two layers. Bader charges analysis evidence that charge transfers of  $0.044e$ ,  $0.086e$ , and  $0.078e$  occurred from the TMDCs to the substrate in the  $\text{CrS}_2/\text{MnO}_2$ ,  $\text{CrSe}_2/\text{MnO}_2$ , and  $\text{CrSSe}/\text{MnO}_2$  systems, respectively. The charge transfer between the Se atom and the S atom in  $\text{CrSSe}/\text{MnO}_2$  is larger than that in  $\text{CrS}_2/\text{MnO}_2$  and  $\text{CrSe}_2/\text{MnO}_2$ , illustrating that the coupling effect between the Janus  $\text{CrSSe}$  monolayer and the magnetic substrate  $\text{MnO}_2$  is stronger than that in  $\text{CrS}_2/\text{MnO}_2$  and  $\text{CrSe}_2/\text{MnO}_2$ . The most robust coupling provides the most substantial magnetic proximity effect, resulting in a distinct improvement in valley polarization.

In fact, the presence of a magnetic substrate not only disrupts the system's inversion symmetry but also triggers weak magnetism within the transition metal atoms.<sup>39,58</sup> In the  $\text{CrS}_2/\text{MnO}_2$ ,  $\text{CrSe}_2/\text{MnO}_2$ , and  $\text{CrSSe}/\text{MnO}_2$  heterojunctions, the magnetic moments of the Cr ions are  $-0.017\mu_B$ ,  $-0.03\mu_B$  and  $0.037\mu_B$ , respectively. The magnetization of Cr atoms induced by a magnetic substrate can lead to the occurrence of spin splitting in band structures without SOC, as depicted in Fig. 6a–c. In  $\text{CrSSe}/\text{MnO}_2$ , the magnetic substrate triggers a more considerable magnetism in  $\text{CrSSe}$ , so the spin splitting near VBM is the most obvious in  $\text{CrSSe}/\text{MnO}_2$  heterojunctions. When taking simultaneously SOC and magnetic proximity effects into consideration, as shown in Fig. 6d, valley polarization will appear in these heterojunctions. In  $\text{CrSSe}/\text{MnO}_2$  heterojunctions, the most significant spin splitting near VBM induced by the magnetism from the magnetic substrate leads to enhanced valley polarization.

To gain comprehensive insights into the spin-valley locked physical properties at the  $K$  and  $K'$  valleys for the  $\text{CrSSe}$  monolayer and the  $\text{CrSSe}/\text{MnO}_2$  heterojunction, we employ the Kubo formula to calculate the Berry curvature, which involves summation from all occupied band contributions:

$$\Omega(k) = - \sum_n \sum_{n' \neq n} f(n) \frac{2\text{Im} \varphi_{nk} [\nu_x |\varphi_{n'k} \varphi_{n'k}| \nu_y |\varphi_{nk}]}{(E_n - E_{n'})^2} \quad (2)$$

where  $n$  and  $n'$  are band structure indices,  $f(n)$ ,  $\nu_{x/y}$ ,  $\varphi_{nk}$ , and  $\varphi_{n'k}$  are the Fermi–Dirac distribution functions of the  $n$ th band

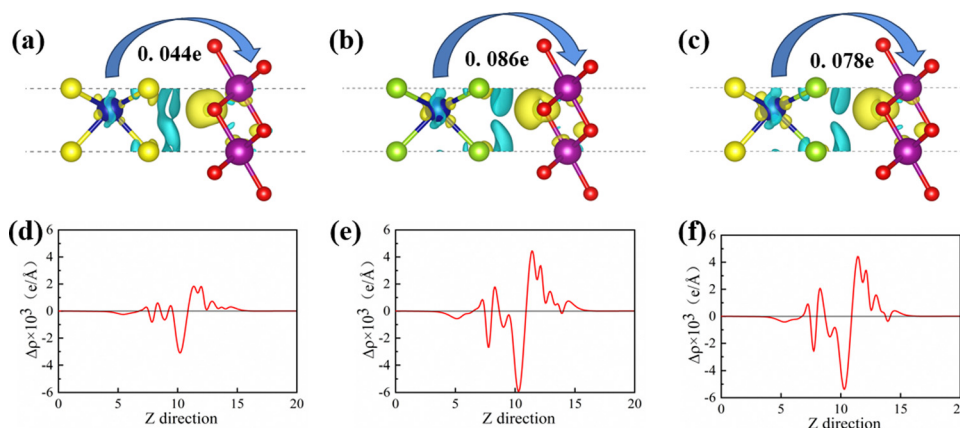


Fig. 5 (a) and (d)  $\text{CrS}_2/\text{MnO}_2$ , (b) and (e)  $\text{CrSe}_2/\text{MnO}_2$ , and (c) and (f)  $\text{CrSSe}/\text{MnO}_2$  differential charge and planar average charge density difference. The yellow and blue regions represent the areas of charge accumulation and disappearance, respectively.



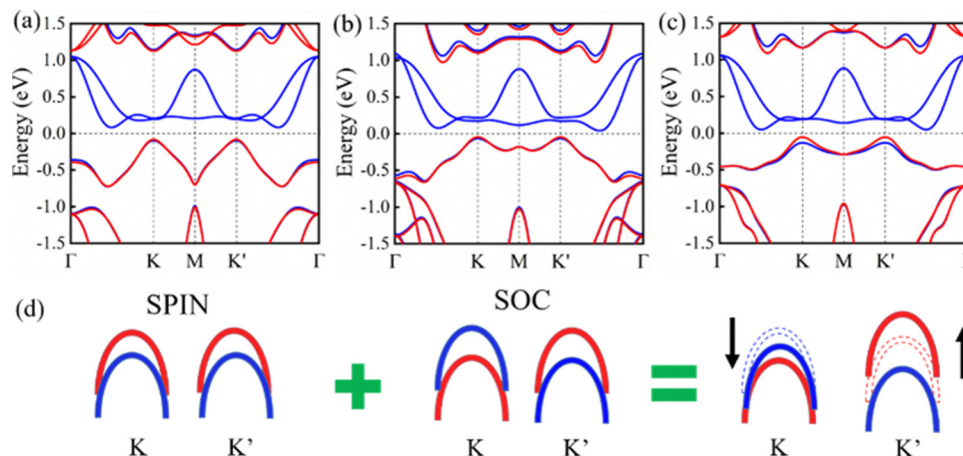


Fig. 6 The spin polarization band of (a)  $\text{CrS}_2/\text{MnO}_2$ , (b)  $\text{CrSe}_2/\text{MnO}_2$ , and (c)  $\text{CrSSe}/\text{MnO}_2$  without SOC. (d) A schematic diagram describing the contributions to the valley polarization of the  $\text{CrX}_2/\text{MnO}_2$  system under SOC and magnetic coexistence.

at point  $k$ , the Dirac electrons along the  $x/y$  direction, and the periodic part of the Bloch wave function with eigenvalues  $E_n$  and  $E_{n'}$ , respectively.

The Berry curvatures of  $\text{CrSSe}$  and  $\text{CrSSe}/\text{MnO}_2$  along high symmetry points are plotted in Fig. 7a. One can see that the Berry curvature of the  $\text{CrSSe}$  monolayer is  $\pm 60.19 \text{ bohr}^2$  at  $K/K'$ , which is comparable to the Berry curvature of monolayer  $\text{MoS}_2$ <sup>14,15</sup> as listed in Table S2 (ESI†). Hence, the absolute values of the  $K$  and  $K'$  valley are identical. In this case, the time-reversal symmetry requires  $\Omega_z(-k) = -\Omega_z(k)$ ; hence, the Berry curvature  $\Omega_z(k)$  is an odd function of the momentum space  $k$ . The peaks of Berry curvatures are located at  $K$  and  $K'$  valleys with equal values but opposite in sign. The Berry curvature of  $\text{CrSSe}/\text{MnO}_2$  is  $-32.94/30.83 \text{ bohr}^2$  at  $K/K'$  as shown in Fig. 7a and b. The absolute values of the  $K$  and  $K'$  valleys are not identical due to the breaking of the time-reversal symmetry along with valley polarization induced by the  $\text{MnO}_2$  magnetic substrate. The identical absolute values for Berry curvatures will cause unequal carriers in the  $K$  and  $K'$  valleys. When doping with a small p-type, holes appear at VBM, which will cause an imbalance of carriers in the  $K$  and  $K'$  valleys. Then, a valley-polarized current will be generated driven by the bias voltage. Moreover, it is clear that the value of Berry curvature has decreased significantly from  $\text{CrSSe}$  to  $\text{CrSSe}/\text{MnO}_2$ , which is similar to the decrease in  $\text{MoS}_2$  and  $\text{MoS}_2/\text{CoO}$ .<sup>59</sup> The decrease

is mainly due to the increase in the bandgap from 0.79 eV for  $\text{CrSSe}$  to 1.16 eV for  $\text{CrSSe}/\text{MnO}_2$  as shown in the layer-resolved band structure in Fig. S3 (ESI†).

Finally, previous studies have shown that electric fields can effectively regulate the coupling between heterojunctions.<sup>37</sup> It is expected to tune the magnetic proximity effects and valley polarization of the  $\text{CrSSe}/\text{MnO}_2$  heterojunction through the electric field. Thus, we applied electric fields on the  $\text{CrSSe}/\text{MnO}_2$  heterojunction to further investigate the electric field effect on valley polarization of the  $\text{CrSSe}/\text{MnO}_2$  heterojunction. The electric field is added from  $-0.6 \text{ eV \AA}^{-1}$  to  $0.6 \text{ eV \AA}^{-1}$  as shown in Fig. 8. Positive values represent the electric field along the  $+z$  direction from the  $\text{MnO}_2$  layer to the  $\text{CrSSe}$  layer, and negative values represent the electric field along the  $-z$  direction. When a positive electric field was imposed, the valley polarization diminished as the electric field intensity increased, as depicted in Fig. 8. At a voltage of  $0.6 \text{ V \AA}^{-1}$ , the valley polarization splitting decreased to 34 meV. In contrast, upon reversing the electric field direction, the valley polarization surged to 81 meV with an electric field intensity of  $-0.4 \text{ V \AA}^{-1}$ . Hence, the electric fields are a practical scheme to tune the valley polarization of heterojunctions. In order to analyse the regulation mechanism of the electric field, we calculated the charge difference and Bader charge analysis. One can notice that the charge transfer changes with the change of electric

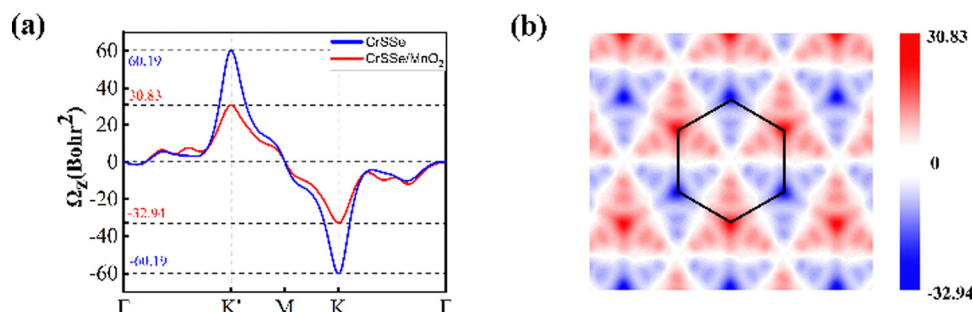


Fig. 7 (a) Berry curvature of Janus  $\text{CrSSe}$  and  $\text{CrSSe}/\text{MnO}_2$  along high symmetry points. (b) Berry curvature of Janus  $\text{CrSSe}/\text{MnO}_2$  in the 2D Brillouin.

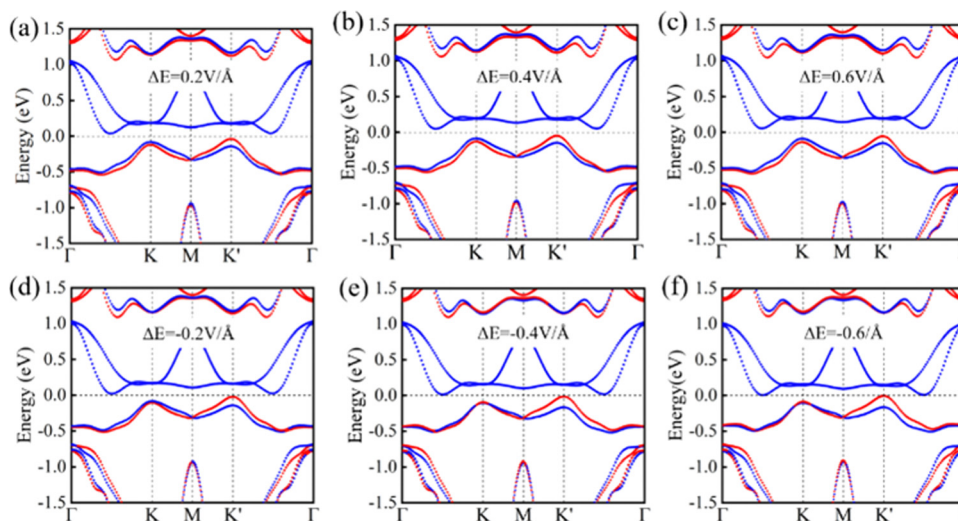


Fig. 8 Spin projection energy bands of CrSSe/MnO<sub>2</sub> heterojunction under different electric field strengths (a) 0.2 V Å<sup>-1</sup>, (b) 0.4 V Å<sup>-1</sup>, (c) 0.6 V Å<sup>-1</sup>, (d) -0.2 V Å<sup>-1</sup>, (e) -0.4 V Å<sup>-1</sup>, (f) -0.6 V Å<sup>-1</sup>.

field as shown in the ESI,<sup>†</sup> Fig. S4. Hence, the evolution of valley polarization with the external electric field is mainly due to the effective regulation of the interlayer coupling by the electric field, thereby changing the magnetic proximity effect and valley polarization.

## 4 Conclusions

In summary, we have investigated the electronic structure and valley-contrasting physics of CrS<sub>2</sub>, CrSe<sub>2</sub>, and CrSSe monolayers by first-principles calculations. Our results indicate that CrS<sub>2</sub>, CrSe<sub>2</sub>, and CrSSe monolayers have intrinsic direct bandgaps of 0.91 eV, 0.70 eV, and 0.79 eV, respectively. The spin-valley coupling in Janus CrSSe is due to the breaking of inversion symmetry and SOC. Furthermore, introducing a magnetic substrate will induce valley polarization because of the magnetic proximity effect. The valley polarization in the CrSSe/MnO<sub>2</sub> heterojunction is more significant than that in CrS<sub>2</sub>/MnO<sub>2</sub> and CrSe<sub>2</sub>/MnO<sub>2</sub> heterojunctions because of the stronger coupling with the magnetic substrate of Janus CrSSe by its high internal electronic field. Furthermore, it was found that the external electric field can further effectively tune the valley polarization splitting. Our results establish a novel foundation for the prospective utilization of valley polarization.

## Conflicts of interest

There are no conflicts to declare.

## Acknowledgements

This work was supported by the National Natural Science Foundation of China (No. 62264010, 12264026, 12004142, and 62201268), the Natural Science Foundation of Jiangxi Province, China (No. 20212BAB211023 and 20224BAB211013) and the

Innovation and Entrepreneurship Leading Talent Plan of Jiangxi Province (No. Jxsq2023101068). LS thanks the Singapore Ministry of Education Academic Research Fund Tier 1 (Grant No. A-8001194-00-00).

## References

- 1 R. Peng, Y. Ma, X. Xu, Z. He, B. Huang and Y. Dai, *Phys. Rev. B*, 2020, **102**, 035412.
- 2 A. R. Akhmerov and C. W. Beenakker, *Phys. Rev. Lett.*, 2007, **98**, 157003.
- 3 A. Rycerz, J. Tworzydło and C. W. J. Beenakker, *Nat. Phys.*, 2007, **3**, 172–175.
- 4 L. Ju, L. Wang, X. Li, S. Moon, M. Ozerov, Z. Lu, T. Taniguchi, K. Watanabe, E. Mueller, F. Zhang, D. Smirnov, F. Rana and P. L. McEuen, *Nat. Commun.*, 2020, **11**, 2941.
- 5 D. Xiao, G. B. Liu, W. X. Feng, X. D. Xu and W. Yao, *Phys. Rev. Lett.*, 2012, **108**, 5.
- 6 H. L. Zeng, J. F. Dai, W. Yao, D. Xiao and X. D. Cui, *Nat. Nanotechnol.*, 2012, **7**, 490–493.
- 7 T. Cao, G. Wang, W. P. Han, H. Q. Ye, C. R. Zhu, J. R. Shi, Q. Niu, P. H. Tan, E. Wang, B. L. Liu and J. Feng, *Nat. Commun.*, 2012, **3**, 5.
- 8 L. L. Tao and E. Y. Tsymlal, *Phys. Rev. B*, 2019, **100**, 161110.
- 9 M. K. Mohanta, F. Is and A. De Sarkar, *Phys. Rev. B*, 2023, **107**, 035429.
- 10 X.-J. Dong, K. Jia, W.-X. Ji, S.-S. Li and C.-W. Zhang, *ACS Appl. Electron. Mater.*, 2023, **5**, 2046–2054.
- 11 J. X. Li, W. Q. Li, S. H. Hung, P. L. Chen, Y. C. Yang, T. Y. Chang, P. W. Chiu, H. T. Jeng and C. H. Liu, *Nat. Nanotechnol.*, 2022, **17**, 721–728.
- 12 Z. Lin, Y. Liu, Z. Wang, S. Xu, S. Chen, W. Duan and B. Monserrat, *Phys. Rev. Lett.*, 2022, **129**, 027401.

- 13 E. C. Castro, D. S. Brandão, H. Bragança, A. S. Martins, F. Riche, A. C. Dias, J. H. Zhao, A. L. A. Fonseca and F. Qu, *Phys. Rev. B*, 2023, **107**, 035439.
- 14 F. Is, R. Ahammed, P. Nandi, A. Rawat and A. De Sarkar, *Appl. Surf. Sci.*, 2023, **611**, 155675.
- 15 J. Zhao, T. Zhang, R. Peng, Y. Dai, B. Huang and Y. Ma, *J. Phys. Chem. Lett.*, 2022, **13**, 8749–8754.
- 16 Z. Huang, J. Wu, C. Wang, S. Yang and F. Ma, *Phys. Rev. B*, 2021, **104**, L041103.
- 17 J. Zhang, S. Jia, I. Kholmanov, L. Dong, D. Er, W. Chen, H. Guo, Z. Jin, V. B. Shenoy, L. Shi and J. Lou, *ACS Nano*, 2017, **11**, 8192–8198.
- 18 J. Yuan, Y. Yang, Y. Cai, Y. Wu, Y. Chen, X. Yan and L. Shen, *Phys. Rev. B*, 2020, **101**, 094420.
- 19 C. Zhang, Y. Nie, S. Sanvito and A. Du, *Nano Lett.*, 2019, **19**, 1366–1370.
- 20 C. Luo, X. Peng, J. Qu and J. Zhong, *Phys. Rev. B*, 2020, **101**, 245416.
- 21 Y. C. Cheng, Z. Y. Zhu, M. Tahir and U. Schwingenschlögl, *Europhys. Lett.*, 2013, **102**, 5.
- 22 Q.-F. Yao, J. Cai, W.-Y. Tong, S.-J. Gong, J.-Q. Wang, X. Wan, C.-G. Duan and J. H. Chu, *Phys. Rev. B*, 2017, **95**, 165401.
- 23 A. Kandemir and H. Sahin, *Phys. Chem. Chem. Phys.*, 2018, **20**, 17380–17386.
- 24 T. V. Vu, H. D. Tong, D. P. Tran, N. T. T. Binh, C. V. Nguyen, H. V. Phuc, H. M. Do and N. N. Hieu, *RSC Adv.*, 2019, **9**, 41058–41065.
- 25 H. U. Din, M. Idrees, A. Albar, M. Shafiq, I. Ahmad, C. V. Nguyen and B. Amin, *Phys. Rev. B*, 2019, **100**, 165425.
- 26 T. Hu, F. Jia, G. Zhao, J. Wu, A. Stroppa and W. Ren, *Phys. Rev. B*, 2018, **97**, 125401.
- 27 W. Y. Tong, S. J. Gong, X. Wan and C. G. Duan, *Nat. Commun.*, 2016, **7**, 13612.
- 28 X.-W. Shen, W.-Y. Tong, S.-J. Gong and C.-G. Duan, *2D Mater.*, 2017, **5**, 011001.
- 29 Y. T. Wang, C. W. Luo, A. Yabushita, K. H. Wu, T. Kobayashi, C. H. Chen and L. J. Li, *Sci. Rep.*, 2015, **5**, 8289.
- 30 K. F. Mak, K. He, J. Shan and T. F. Heinz, *Nat. Nanotechnol.*, 2012, **7**, 494–498.
- 31 H. Zeng, J. Dai, W. Yao, D. Xiao and X. Cui, *Nat. Nanotechnol.*, 2012, **7**, 490–493.
- 32 Y. Wang, W. Wei, F. Li, X. Lv, B. Huang and Y. Dai, *Mater. Horiz.*, 2021, **8**, 244–249.
- 33 G. Aivazian, Z. Gong, A. M. Jones, R.-L. Chu, J. Yan, D. G. Mandrus, C. Zhang, D. Cobden, W. Yao and X. Xu, *Nat. Phys.*, 2015, **11**, 148–152.
- 34 D. MacNeill, C. Heikes, K. F. Mak, Z. Anderson, A. Kormanyos, V. Zolyomi, J. Park and D. C. Ralph, *Phys. Rev. Lett.*, 2015, **114**, 037401.
- 35 R. Peng, Y. Ma, S. Zhang, B. Huang and Y. Dai, *J. Phys. Chem. Lett.*, 2018, **9**, 3612–3617.
- 36 Y. C. Cheng, Q. Y. Zhang and U. Schwingenschlögl, *Phys. Rev. B: Condens. Matter Mater. Phys.*, 2014, **89**, 155429.
- 37 I. Khan, B. Marfoua and J. Hong, *npj 2D Mater. Appl.*, 2021, **5**, 10.
- 38 T. Norden, C. Zhao, P. Zhang, R. Sabirianov, A. Petrou and H. Zeng, *Nat. Commun.*, 2019, **10**, 4163.
- 39 Z. Zhang, X. Ni, H. Huang, L. Hu and F. Liu, *Phys. Rev. B*, 2019, **99**, 115441.
- 40 J. Qi, X. Li, Q. Niu and J. Feng, *Phys. Rev. B: Condens. Matter Mater. Phys.*, 2015, **92**, 121403.
- 41 Q. Zhang, S. A. Yang, W. Mi, Y. Cheng and U. Schwingenschlögl, *Adv. Mater.*, 2016, **28**, 959–966.
- 42 X. Wang and J.-Y. You, *Mater. Today Electron.*, 2023, **5**, 100051.
- 43 H. Zheng, B. Wu, C.-T. Wang, S. Li, J. He, Z. Liu, J.-T. Wang, G. Yu, J.-A. Duan and Y. Liu, *Nano Res.*, 2023, **16**, 10580–10586.
- 44 L. Xu, M. Yang, L. Shen, J. Zhou, T. Zhu and Y. P. Feng, *Phys. Rev. B*, 2018, **97**, 041405.
- 45 G. Yang, J. Li, H. Ma, Y. Yang, C. Li, X. Mao and F. Yin, *Phys. Rev. B*, 2018, **98**, 235419.
- 46 G. Kresse and J. Furthmüller, *Phys. Rev. B: Condens. Matter Mater. Phys.*, 1996, **54**, 11169–11186.
- 47 P. E. Blochl, *Phys. Rev. B: Condens. Matter Mater. Phys.*, 1994, **50**, 17953–17979.
- 48 J. P. Perdew, K. Burke and M. Ernzerhof, *Phys. Rev. Lett.*, 1996, **77**, 3865–3868.
- 49 V. I. Anisimov, A. I. Poteryaev, M. A. Korotin, A. O. Anokhin and G. Kotliar, *J. Phys.: Condens. Matter*, 1997, **9**, 7359–7367.
- 50 Q. Wei, D. Chen, Y. Cai, L. Shen, J. Xu, J. Yuan, Y. Chen and X. Yan, *J. Supercond. Novel Magn.*, 2022, **35**, 787–794.
- 51 A. A. Mostofi, J. R. Yates, Y.-S. Lee, I. Souza, D. Vanderbilt and N. Marzari, *Comput. Phys. Commun.*, 2008, **178**, 685–699.
- 52 A. Togo and I. Tanaka, *Scr. Mater.*, 2015, **108**, 1–5.
- 53 K. Chen, J. Deng, Y. Yan, Q. Shi, T. Chang, X. Ding, J. Sun, S. Yang and J. Z. Liu, *npj Comput. Mater.*, 2021, **7**, 79.
- 54 H. Zhang, L.-M. Liu and W.-M. Lau, *J. Mater. Chem. A*, 2013, **1**, 10821–10828.
- 55 D. Wines, K. Saritas and C. Ataca, *J. Phys. Chem. C*, 2022, **126**, 5813–5821.
- 56 Q. Li, K.-Q. Chen and L.-M. Tang, *Phys. Rev. Appl.*, 2020, **13**, 014064.
- 57 B. Zhou, Z. Li, J. Wang, X. Niu and C. Luan, *Nanoscale*, 2019, **11**, 13567–13575.
- 58 T. Hu, G. Zhao, H. Gao, Y. Wu, J. Hong, A. Stroppa and W. Ren, *Phys. Rev. B*, 2020, **101**, 125401.
- 59 G. Yang, J. Li, Z. Liu, C. Li and X. Mao, *Phys. Chem. Chem. Phys.*, 2019, **21**, 15151–15156.